

Research Article

Influence of Water Saturation on Adsorption Behavior at Liquid-Liquid Interfaces in Unsaturated Porous Media

Yan Zhu ¹, Ziteng Cui ², Kun Li,³ Chaoqi Wang ¹, Zhao Li ¹, Xueyi Zhang ¹,
and Zhi Dou ¹

¹School of Earth Sciences and Engineering, Hohai University, Nanjing 210098, China

²China Water Investment Co., LTD., Beijing 100053, China

³Shandong Water Transfer Project Operation and Maintenance Center, Jinan 250000, China

Correspondence should be addressed to Zhao Li; lizhao1990@hhu.edu.cn and Zhi Dou; dz.uriah@gmail.com

Received 21 July 2023; Revised 6 September 2023; Accepted 12 October 2023; Published 9 November 2023

Academic Editor: Bao Jia

Copyright © 2023 Yan Zhu et al. This is an open access article distributed under the Creative Commons Attribution License, which permits unrestricted use, distribution, and reproduction in any medium, provided the original work is properly cited.

Adsorption reaction in unsaturated porous media is of great importance for soil and groundwater remediation. In this study, the influence of the Peclet number (Pe) and water saturation on adsorption behavior at liquid-liquid interfaces was quantitatively investigated. The pore-scale reactive transport in unsaturated porous media was directly simulated. The Navier-Stokes equations, the surface transfer and adsorption reaction equations, and the advection-diffusion equation (ADE) were coupled to obtain the flow and concentration fields. The results showed that water saturation had a significant influence on the complexity of the flow field. A nonmonotonic relationship was found between water saturation and the uniformity of the flow field. Peclet number had little influence on the maximum adsorption. On the other hand, the adsorption time showed a nearly linear relationship with the Peclet number and increased with increasing Peclet number. Additionally, a nonlinear relationship was found between water saturation and the maximum adsorption. As water saturation increased, the maximum adsorption tended to increase to a peak and then decrease. The peak of the maximum adsorption occurred at $Pe = 5$, $S_w = 0.458$, and the shortest adsorption time was observed at $S_w = 0.902$. However, the difference in adsorption times for saturations of 0.458 and 0.698 was not significant and was only about 20 PV difference.

1. Introduction

Soil is an important resource for human survival and a site for various reactions in groundwater. Surface soils are mostly unsaturated porous media subject to natural influences. In recent years, it has become evident that uncontrolled use and immature environmental regulations have led to a variety of ecological and environmental problems. Pollutants such as organic matter, heavy metals, pesticides, and fertilizers led to long-term soil pollution. In addition, soil pollution caused significant pollution of groundwater due to adsorption reactions at the soil surface and hydrodynamic influences on the groundwater system [1–5]. Therefore, understanding and applying reactive solute transport in unsaturated porous media and their internal adsorption reactions are crucial for soil and groundwater remediation.

Solute transport in porous media has been widely studied [6–9]. As in previous studies, solute transport research focused on the macroscopic scale. Transport processes in porous media were studied by constructing unit bodies and using averaging parameters to make macroscopic generalizations about their relevant properties. Wu et al. [10] determined the topology of spatial structure between particles of agar bead-filled beds under water-saturated conditions using magnetic resonance imaging (MRI). Wang et al. [11] studied the influence of soil anisotropy on solute transport. Pore-scale studies have made significant progress in recent years due to advances in computer technology and the refinement of numerical simulation techniques. Current methods for determining microscopic pore structure in porous media include physical imaging techniques and numerical methods. Zhou and Xiao [12] proposed a method to reconstruct 3D

multiphase rock models using a combination of computerized tomography (CT) and multiple features to study simulated fracture formation and obtained better results compared to experimental data. Scanning electron microscope (SEM) is also widely used; Liu et al. [13] and Zhao et al. [14] produced gray-scale images to refine the microstructure and quantify the characteristic parameters of the pore structure. Luo et al. [15] combined process-driven three-dimensional (3D) digital rock modeling with fractal analysis to create a digital rock model of simulated sandstone. Zhao et al. [16] determined the porosity of residual granite beds under external loading by CT scanning and derived the microstructural evolution process. However, due to the economic and technical limitations of the physical imaging method, the numerical simulation method has been used more frequently.

Although considerable efforts have been made in the field of solute transport in recent years, many studies have addressed only partial aspects that have been covered, especially in reactive solute transport problems [17–21]. Unsaturated brucite [$\text{Mg}(\text{OH})_2$] bearing column experiments have been used to evaluate the influence of the change in reactive mineral surface area, water content, precipitation of hydrous Mg carbonate, and gas distribution on the reaction of brucite [$\text{Mg}(\text{OH})_2$] with CO_2 gas [22, 23]. The results confirmed that conventional geometric surface updating models do not adequately represent the observed reaction process during the carbonation of brucite. Raoof et al. [24] presented a pore network modeling tool capable of simulating fluid flow and reactive and adsorptive transport of multiple components under saturated and differentially saturated conditions. Jiménez-Martínez et al. [25] pointed out mechanisms by which the mixing of an invading fluid with the resident fluid is considerably enhanced as saturation decreases, and the effective reactivity is much greater than under saturated conditions. Mixing-driven reactions in porous media are ubiquitous, but predicting where and how fast the reactions occur has been a tremendous challenge due to the complex and nonuniform nature of porous media flows [26]. Dou et al. [27] developed a pore-level numerical simulation model to investigate the saturation dependence of mass transfer in unsaturated porous residual media and the influence of saturation topography on mass transfer. They discovered a nonmonotonic relationship between dispersivity and residual saturation. However, the reactive properties at the liquid-liquid interface are neglected. Especially for adsorption, Yue et al. [28] studied the adsorption and desorption of the herbicide atrazine on soils, which is dominated by surface adsorption at low concentrations and influenced by adsorption sites on the adsorption surface. According to Lyu et al. [29], the spherical structure and ultrahigh surface ratio of the extremely efficient catalyst were studied to make it more efficient and stable. Thus, interfacial adsorption is the key to soil remediation, and the research combining unsaturated porous media with interfacial adsorption will receive more attention.

In this study, the complex pore structure was reconstructed to simulate the reactive solute transport in unsaturated porous media considering adsorption reactions at the interfaces at the pore scale. An immiscible two-phase trans-

port (ITPT) model was used to construct the geometric model of the unsaturated porous media with different water saturations. The Navier-Stokes equation, the surface transfer and adsorption reaction equations, and the advection-diffusion equation (ADE) were coupled and applied to the geometric model using COMSOL Multiphysics. We investigated the influence of water saturation on the flow field and quantitatively evaluated the uniformity of the flow velocity distribution. The influence of the Peclet number and water saturation on adsorption behavior at liquid-liquid interfaces was analyzed.

2. Materials and Methods

2.1. Unsaturated Porous Media Generation. A series of regular circles with different radii were simulated as solid particles in the porous media. The microscopic pore structure of saturated porous media particles was generated using the method described by Dou et al., i.e., a single porous medium with target porosity is generated in a specific region [30]. It should be noted that the size of the solid particles must be appropriate. To this end, the radius of the particle size should not only be within the range where the mean particle size and the standard deviation of the particle size distribution were usually controlled but also followed a truncated log-normal distribution. In this study, the radius ranged from 0.3 mm to 0.9 mm and was randomly distributed in a size range of 41×18 mm. The coefficient of variation (COV) was equal to 0.25, and the porosity of the generated porous media was set to 0.42. Due to the random distribution of particles and heterogeneous radius sizes, the internal spatial structure of the porous media was complex. Therefore, the porous media were considered heterogeneous in this study.

Our numerical simulations were based on four porous medium topologies with different water saturations ($S_w = 0.458$, $S_w = 0.698$, $S_w = 0.902$, and $S_w = 1.000$). The topology was determined by an ITPT model consisting of immiscible two-phase flows at the pore scale of Dou et al. [27]. Transport at the immiscible boundary was tracked using the phase field method (PFM). Trichloroethylene (TCE) was assumed to be the nonwetting phase fluid, and water was injected as the wetting phase fluid. The porous medium was first saturated with TCE and then injected with water at three rates to displace the TCE. In the end, we obtained models with different water saturations. As shown in Figure 1, the solid grains were shown in white. The liquid in the nonwetting phase was shown in gray, the blue areas showed the flow paths, and the interface between gray and blue is the liquid-liquid interface, where the adsorption and desorption reaction occurred.

2.2. Fluid Flow and Adsorptive Transport Modeling. To solve the mass transfer problem in unsaturated porous media, it is necessary to couple the groundwater flow field with the mass transfer concentration field. The mathematical fields of the reactive adsorption process must also be coupled with the two aforementioned fields to account for the adsorption reaction of solutes with the internal residual non-wetting phase.

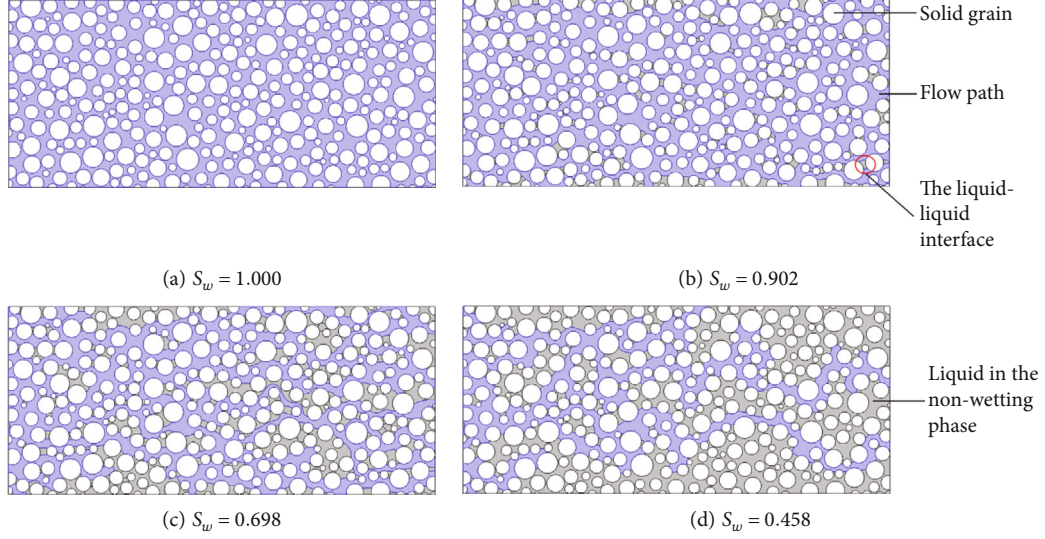


FIGURE 1: Topologies of porous media with different water saturations. The solid grains were shown in white. The liquid in the nonwetting phase was shown in gray, the blue areas showed the flow paths, and the interface between gray and blue is the liquid-liquid interface, where the adsorption and desorption reaction occurred.

To simulate water flow in unsaturated porous media, we used the Navier-Stokes equation as the control equation for water flow.

$$\begin{aligned} \rho g \nabla \varphi + \mu \nabla u &= 0, \\ \nabla \cdot u &= 0, \end{aligned} \quad (1)$$

where ρ [$\text{kg} \cdot \text{m}^{-3}$] is the density of water, g [$\text{m} \cdot \text{s}^{-2}$] is the acceleration of gravity, and φ [m] represents the water head. $\mu = 1 \times 10^{-3} \text{ kg} \cdot (\text{m} \cdot \text{s})^{-1}$ is the dynamic viscosity coefficient of water, and u [$\text{m} \cdot \text{s}^{-1}$] is the velocity.

The adsorption/desorption reaction at the interface of unsaturated porous media can be described as



where the forward reaction rate is k_f , the reverse reaction rate is k_r , A is the molecular material in the solute, and A_s is the molecular material adsorbed on the surface.

In this study, adsorption in a single molecular layer was used for the reaction interface, and molecular forces between adsorbed molecules were neglected to account for adsorption at the interface during solute transport. According to the Langmuir hypothesis of adsorption in a single molecular layer, the adsorption capacity at all adsorbable interfaces was the same because the interface was homogeneous throughout. Therefore, the adsorption and desorption processes were in a dynamic equilibrium state during solute transport.

Assuming that θ is the percentage of the surface covered by adsorbed molecules, the percentage of the free zone is $1 - \theta$. According to Langmuir's theory of monolayer adsorption, the desorption rate of molecules, r_{des} ($\text{mol}/(\text{m}^2 \cdot \text{s})$), was proportional to θ and equal to $k_r \theta$, where k_r was constant at a

TABLE 1: Calculation parameter settings.

Symbols	Parameter name	Unit	Value
c_0	Initial concentration	mol/m^3	0.002
k_{ads}	Adsorption rate constants	$\text{m}^3/(\text{s} \cdot \text{mol})$	4.12
k_{des}	Desorption rate constant	1/s	2E-4
Γ_s	Active site concentration	mol/m^2	2E-6
D_s	Surface diffusivity	m^2/s	1E-11
D	Reactant diffusivity	m^2/s	1E-9

constant temperature. The adsorption rate of molecules was proportional to the percentage of free zone $1 - \theta$ and the rate at which the molecule collided with the surface. The collision rate was in turn proportional to the partial pressure of the substance P_A (Pa). The adsorption rate ($\text{mol}/(\text{m}^2 \cdot \text{s})$) was therefore expressed as r_{ads} , which was equal to $k_f P_A (1 - \theta)$. The k_r was constant at a constant temperature.

To establish the equation by the concentrations, the following substitutions are made.

$$\theta = \frac{c_s}{\Gamma_s}, \quad (3)$$

$$P_A = cRT, \quad (4)$$

where we set the in-domain concentration of A to c [$\text{mol} \cdot \text{m}^{-3}$] and the surface concentration to c_s [$\text{mol} \cdot \text{m}^{-3}$]. $\Gamma_s = 2 \times 10^{-6} \text{ mol} \cdot \text{m}^{-2}$ is the total concentration of the surface that can be covered by the adsorbed molecules, R [$\text{J} \cdot (\text{mol} \cdot \text{K})^{-1}$] is the gas constant, and T [K] is the temperature.

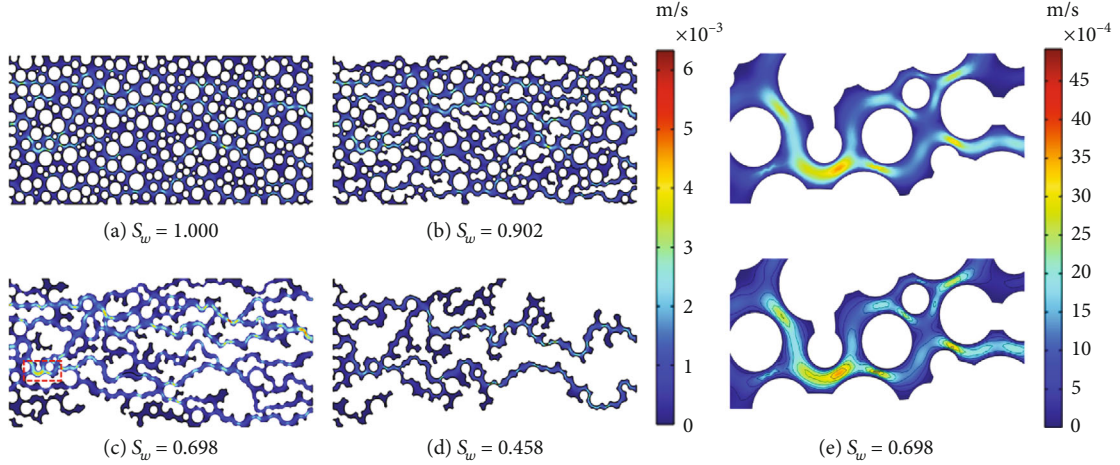


FIGURE 2: The flow fields in saturated (a) and unsaturated porous media (b–d) and the distribution of water flow (e).

Eq. (3) and Eq. (4) were used to derive the adsorption and desorption rates.

$$\gamma_{\text{des}} = k_{\text{des}}c_s, \quad (5)$$

$$\gamma_{\text{ads}} = k_{\text{ads}}c(\Gamma_s - c_s), \quad (6)$$

where the rate constant for the desorption reaction $k_{\text{des}} = 2 \times 10^{-4} \text{ s}^{-1}$ and the rate constant for the adsorption reaction $k_{\text{ads}} = 4.12 \text{ m}^3 \cdot (\text{mol} \cdot \text{s})^{-1}$.

This leads to the equations for surface transfer and adsorption.

$$\frac{\partial C_s}{\partial t} + \nabla \cdot (-D_s \nabla C_s) = k_{\text{ads}}c(\Gamma_s - c_s) - k_{\text{des}}c_s. \quad (7)$$

The nonuniform velocity field of groundwater flow in unsaturated porous media and the surface reaction rate can be derived from Eq. (5) and Eq. (6), which are inserted into ADE to obtain the following equation.

$$\frac{\partial c}{\partial t} + \nabla \cdot (-D \nabla c + cu) = 0, \quad (8)$$

where the surface diffusion coefficient $D_s = 1 \times 10^{-11} \text{ m}^2 \cdot \text{s}^{-1}$ and the reactant diffusivity $D = 1 \times 10^{-9} \text{ m}^2 \cdot \text{s}^{-1}$.

2.3. Numerical Modeling Strategy and Setup. COMSOL Multiphysics finite element software (COMSOL Inc., Burlington, MA, USA) was used to simulate water flow, solute transport, and adsorption at the interface using. The model was set up with a constant pressure outlet boundary on the right and a constant pressure inlet boundary on the left. The particle boundary and the upper and lower boundaries of the geometric model were set as slip-free boundaries. The slip-free boundary condition is a central part of the boundary conditions used in fluid dynamics. It assumes that the fluid in direct contact with a solid surface adheres to that surface and has the same velocity as the surface. In other words, the velocity of the fluid directly at the boundary is zero. The inclusion of the slip-free boundary condition greatly

TABLE 2: Velocity uniformity indexes.

Water saturation	CV	γ_v
$S_w = 1.000$	1.0193	0.5943
$S_w = 0.902$	0.9803	0.6037
$S_w = 0.698$	1.0921	0.5427
$S_w = 0.458$	1.1623	0.5138

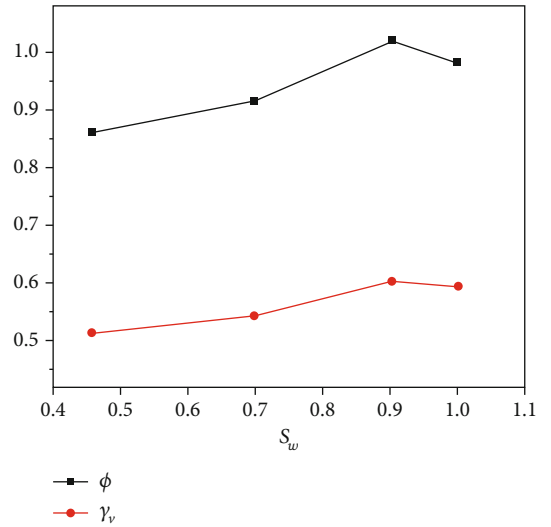


FIGURE 3: Velocity uniformity at different water saturations. The ϕ ($\phi = 1/\text{CV}$) and γ_v value showed the same trend, increased, and then decreased as water saturation decreased.

simplifies the mathematical representation of the interactions between different materials and their corresponding surfaces. Different pressure differences were set for the different models to characterize the distribution of water pressure, and the water flowed under the initial pressure difference.

As a fundamental requirement for solute transport, it was important to determine the principles controlling the fluctuation of the flow field in porous media. The Navier-

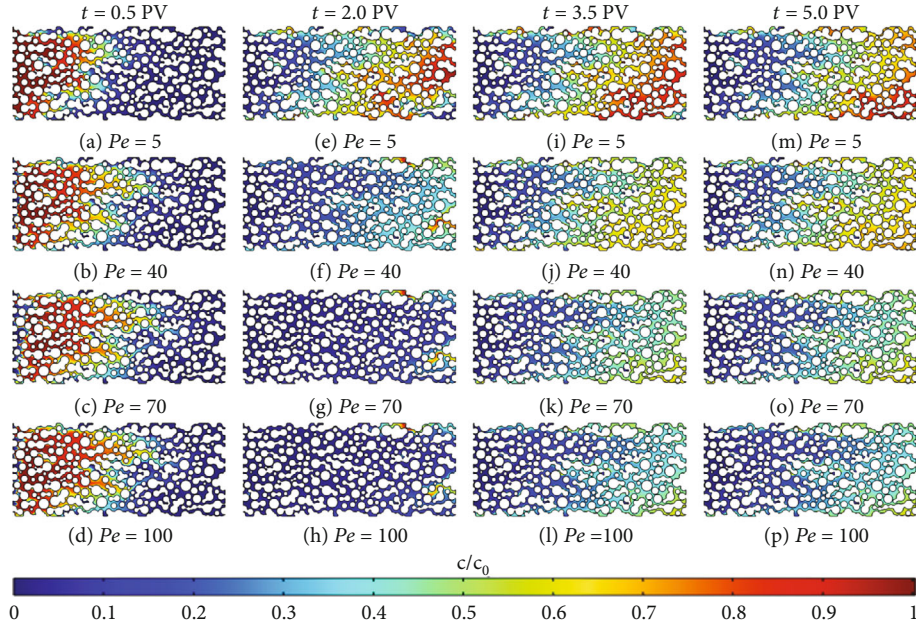


FIGURE 4: Reactive transport processes in porous media ($S_w = 0.902$). c/c_0 is the dimensionless concentration.

Stokes equation was coupled with the advection-diffusion equation to regulate the flow field. Water flow is controlled by applying the pressure difference (5 Pa) between the inlet and outlet. To simulate adsorption behavior at liquid-liquid interfaces in unsaturated porous media in the pore structure, the solute with the specific concentration ($c_0 = 2 \times 10^{-3} \text{ mol/m}^3$) was injected along the inlet boundary. At the same time, the corresponding reaction rate constants were determined to represent the adsorption reaction at the interface. The specific parameters are given in Table 1.

3. Results and Discussion

3.1. Impact of Water Saturation on the Flow Fields. Figure 2 shows the distribution of the flow field at different water saturations. It can be seen that the distribution of the flow field was complex, and there was a clear phenomenon of preferential flow. This preferential flow generally occurred between two groups of solid particles that formed the dominant channel and were almost parallel to each other. Compared with the flow velocity in the surrounding area, the dominant channel had a higher velocity, and the flow direction was approximately parallel to the water flow. At the same water saturation, the distribution of dominant channels was complex and random due to the influence of pore structure and the distribution of water. Multiple dominant channels may be connected at one location to form a larger dominant channel or separated at another location to form multiple smaller dominant channels. This random separation creates the heterogeneity of the flow field in porous media. In Figure 2, it can be seen that water saturation has a significant influence on the occurrence of connectivity and separation of the dominant flow. The strongest connectivity and separation occurred in the least saturated porous media.

To investigate the phenomenon of preferential flow, the location of the peak velocity of the flow field was selected

for magnification. In Figures 2(a)–2(d), it can be seen that there was a clear phenomenon in the velocity distribution of the flow field in the pore structure: the peak velocity was located on the line connecting the centers of the circles of two groups of nearly parallel solid particles, and the velocity decreased in all directions with the peak velocity as the center. In Figure 2(e), the water flowed in the dominant channel. As the distance between the two groups of solid particles decreased, the flow velocity peaked. However, due to the random distribution of the pores, the particles differed greatly in size, and the dominant channel was divided into two parts, forming two tributaries that continued the flow.

In this study, the profiles of flow velocity were determined to quantitatively evaluate the uniformity of flow velocity. The coefficient of variation [31] and uniformity index [32] were used for the comprehensive analysis.

The coefficient of variation (CV) is dimensionless. It reflects the degree of dispersion of the flow velocity compared to the mean flow velocity and exhibits a negative relationship with the flow field uniformity.

$$S = \sqrt{\frac{1}{n-1} \sum_{i=1}^n (V_i - \bar{V})^2}, \quad (9)$$

$$CV = \frac{S}{\bar{V}} \times 100\%,$$

where S is the standard deviation. V_i [$\text{m}\cdot\text{s}^{-1}$] is the velocity value at i , and \bar{V} [$\text{m}\cdot\text{s}^{-1}$] is the mean velocity. n represents the total number of sample points obtained.

As the crucial evaluation parameter of the flow field uniformity, the uniformity index (γ_i) shows the flow velocity distribution across the entire section. The range of values is 0 to 1.

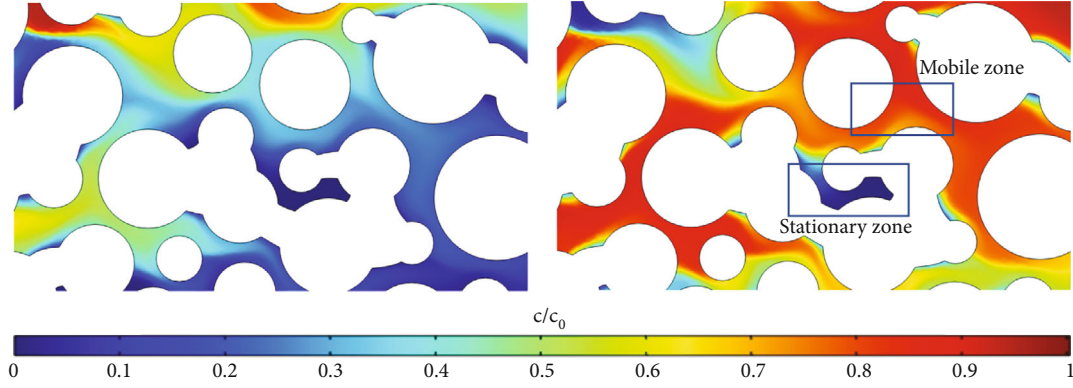


FIGURE 5: Distribution of stationary and mobile zones in the concentration field.

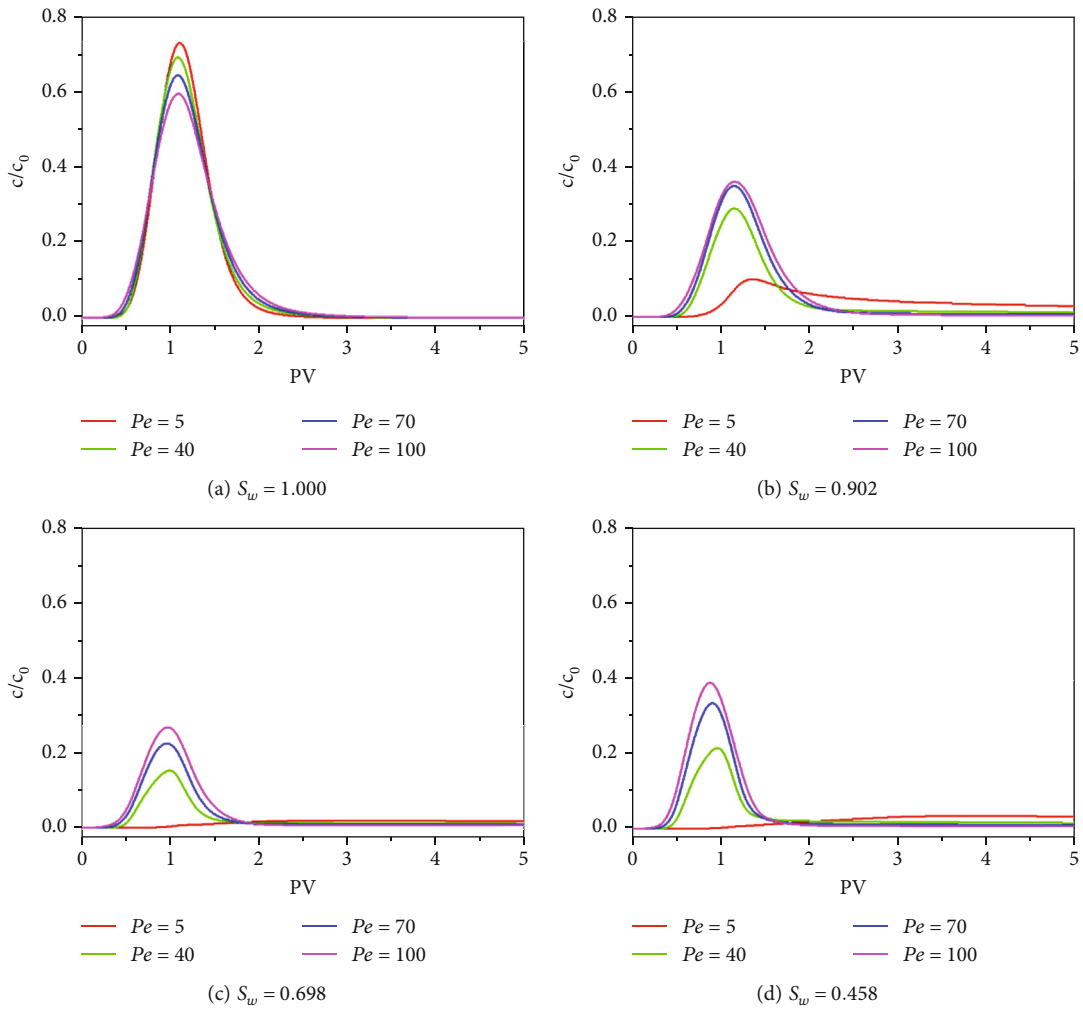


FIGURE 6: Breakthrough curves at different Peclet numbers.

$$\gamma_v = 1 - \frac{1}{2n} \sum_{i=1}^n \frac{\sqrt{(V_i - \bar{V})^2}}{\bar{V}}. \quad (10)$$

According to Table 2, the CV were all close to 1.000 and did not significantly change with water saturation. Mean-

while, the γ_v values at four water saturation were all more than 0.5000. Poor uniformity of the flow field was discovered after a thorough investigation of the two indicators. We plotted the relationship between uniformity and water saturation, as seen in Figure 3, in order to clearly analyze the relationship. Since the CV was inversely related to uniformity, we

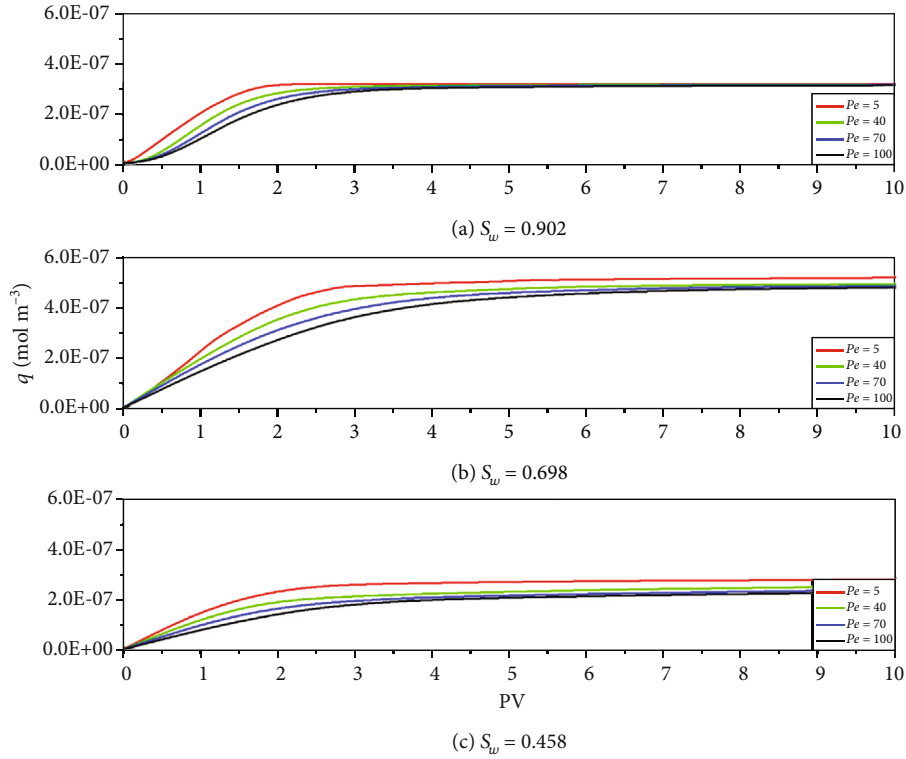


FIGURE 7: The influence of contact time on the adsorbed amount at different Peclet numbers. The adsorbed amount varied regularly with time and gradually increased to equilibrium as time increased.

TABLE 3: The values of the saturated adsorption and adsorption time at different Peclet numbers and water saturations.

Peclet number	Water saturation	q_{\max} (mol/m^3)	T (PV)
Pe = 5	$S_w = 0.902$	$3.1730E-7$	2.8093
	$S_w = 0.698$	$5.3186E-7$	17.005
	$S_w = 0.458$	$2.9541E-7$	43.079
Pe = 40	$S_w = 0.902$	$3.1694E-7$	14.363
	$S_w = 0.698$	$5.3157E-7$	131.91
	$S_w = 0.458$	$2.8396E-7$	118.67
Pe = 70	$S_w = 0.902$	$3.1424E-7$	9.2185
	$S_w = 0.698$	$5.3154E-7$	220.02
	$S_w = 0.458$	$2.8405E-7$	208.67
Pe = 100	$S_w = 0.902$	$3.1434E-7$	12.945
	$S_w = 0.698$	$5.3137E-7$	298.81
	$S_w = 0.458$	$2.8421E-7$	300.9

used the inverse of CV ($\phi = 1/CV$) and the γ_v value to effectively indicate the magnitude of the flow field uniformity. The ϕ and γ_v value showed the same trend, increased, and then decreased as water saturation decreased. In other words, the flow uniformity showed a nonmonotonic relationship as water saturation decreased.

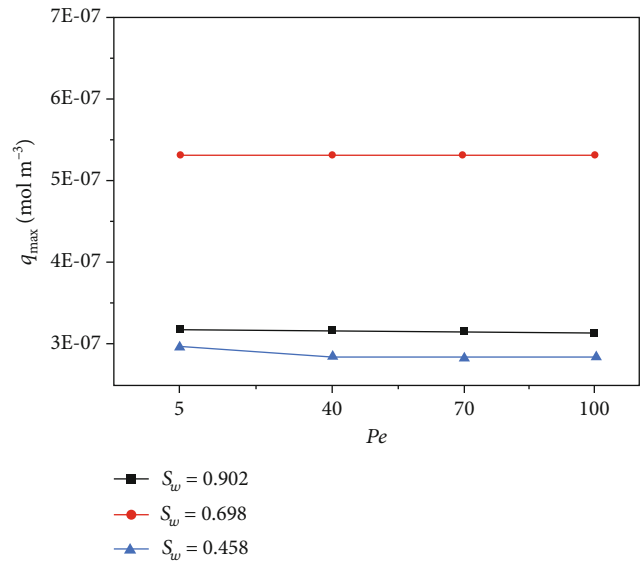


FIGURE 8: The values of the maximum adsorption at different Peclet numbers. Peclet number had little influence on the maximum adsorption.

3.2. Impact of the Peclet Number on Adsorption Behavior at Liquid-Liquid Interfaces. Four different Peclet numbers ($Pe = 5$, $Pe = 40$, $Pe = 70$, and $Pe = 100$) were set at the same water saturation to investigate the influence of different

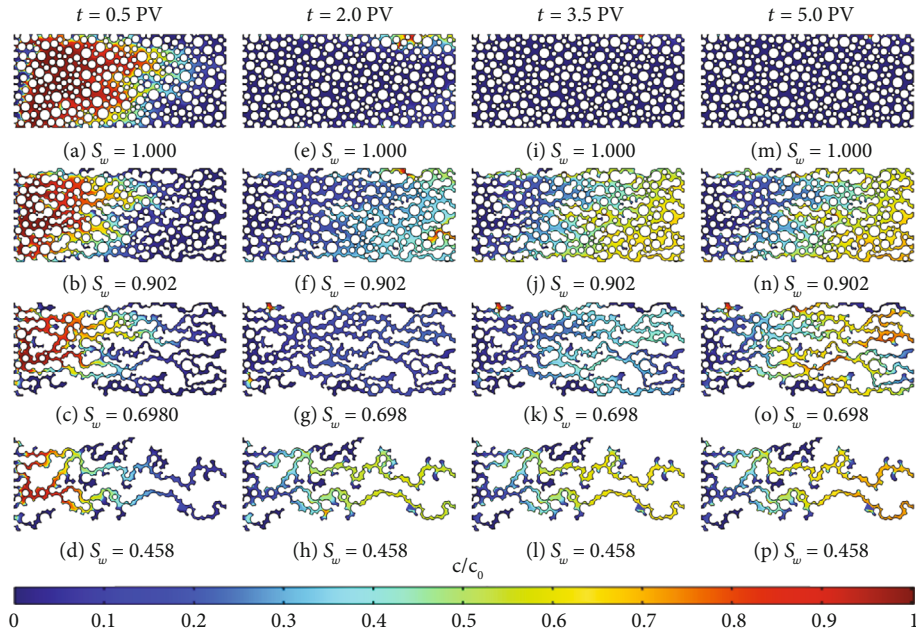


FIGURE 9: Reactive transport processes in porous media ($Pe = 40$). c/c_0 is the dimensionless concentration.

Pecllet numbers on reactive transport in unsaturated porous media.

It is evident from Figure 4 that the Pecllet number has a significant influence on reactive transport in unsaturated porous media. One or more preferential fronts with high transport rates occurred in the porous media. These fronts were distributed at higher concentrations when the solutes were still at low concentrations in other areas. During solute transport, the solutes first occupied the larger pores and then diffused toward the smaller pores, with several larger pores together forming the preferred channel for solute transport. Large pore channels had a better connection and higher flow velocity than small pore channels, which allowed large pores to load up with solutes at higher head pressures. However, the velocity in small pores was significantly lower than in large pores that form the preferred channels because small pore channels were mainly filled by diffusion due to weak advection. The direction of movement of the fronts formed by solute transport was affected by the distribution of the larger pore spaces, and the fronts moved along the channels formed mainly by the larger pore spaces.

Considering four groups of models of unsaturated porous media with different Pecllet numbers at the same water saturation, we find the following: at 0.5 PV, all the solute was injected, and the concentration near the left inlet was in the higher range, but some of the ranges lagged behind the concentration changes in the surrounding area. Then, the injection of water is continued. At 2 PV, the solutes had essentially flowed out of the right outlet, and the entire region was in a state of zero concentration. However, some areas still had a high residual solute concentration and lagged behind the change in the concentration center. Because of this phenomenon, these areas were referred to as “stationary zones.” Stationary zones were usually made up of smaller pores or dead-end pores with a slow flow

velocity and weak advection that relied on diffusion filling of solute molecules, so these areas lagged behind changes in the surrounding area as if they were stopped. In contrast, there were also “mobile zones” (see Figure 5).

In the following simulation period, the solutes in the stationary zone were largely dispersed by the continuous input of water. However, due to adsorption, a large number of solutes were adsorbed on the surface of the nonwetting liquid phase in the initial phase. The desorption reaction at the interface gradually became visible due to the repulsion of water, as shown by the results in Figures 4(i)–4(p). It can be observed that the desorption is strongly affected by the Pecllet number. For the models with unsaturated porous media geometry and smaller Pecllet number, significantly more solute was desorbed from the surface of the nonwetting liquid, while less was desorbed for the larger Pecllet number.

In this study, the outlet boundary was used as the location for calculating the concentration of the breakthrough curves. The simulation time was set to 5 PV in the COMSOL Multiphysics software (0–0.5 PV for solute injection and 0.5–5 PV for water injection), and this was used as the horizontal coordinate. The expression for the dimensionless concentration was as follows.

$$\frac{c}{c_0} = \frac{\int_0^{L_y} (c\bar{u})dy}{\int_0^{L_y} (c_0\bar{u})dy}, \quad (11)$$

where the solute concentration is c [$\text{mol}\cdot\text{L}^{-1}$] and the initial concentration of solute is c_0 [$\text{mol}\cdot\text{L}^{-1}$]. The length of the outlet boundary is L_y . The average velocity of water flow is \bar{u} .

The breakthrough curves for different Pecllet numbers at four different water saturations are shown in Figure 6. All BTCs at the same water saturation showed typical characteristics of anomalous transport behavior (e.g., long tails of BTCs).

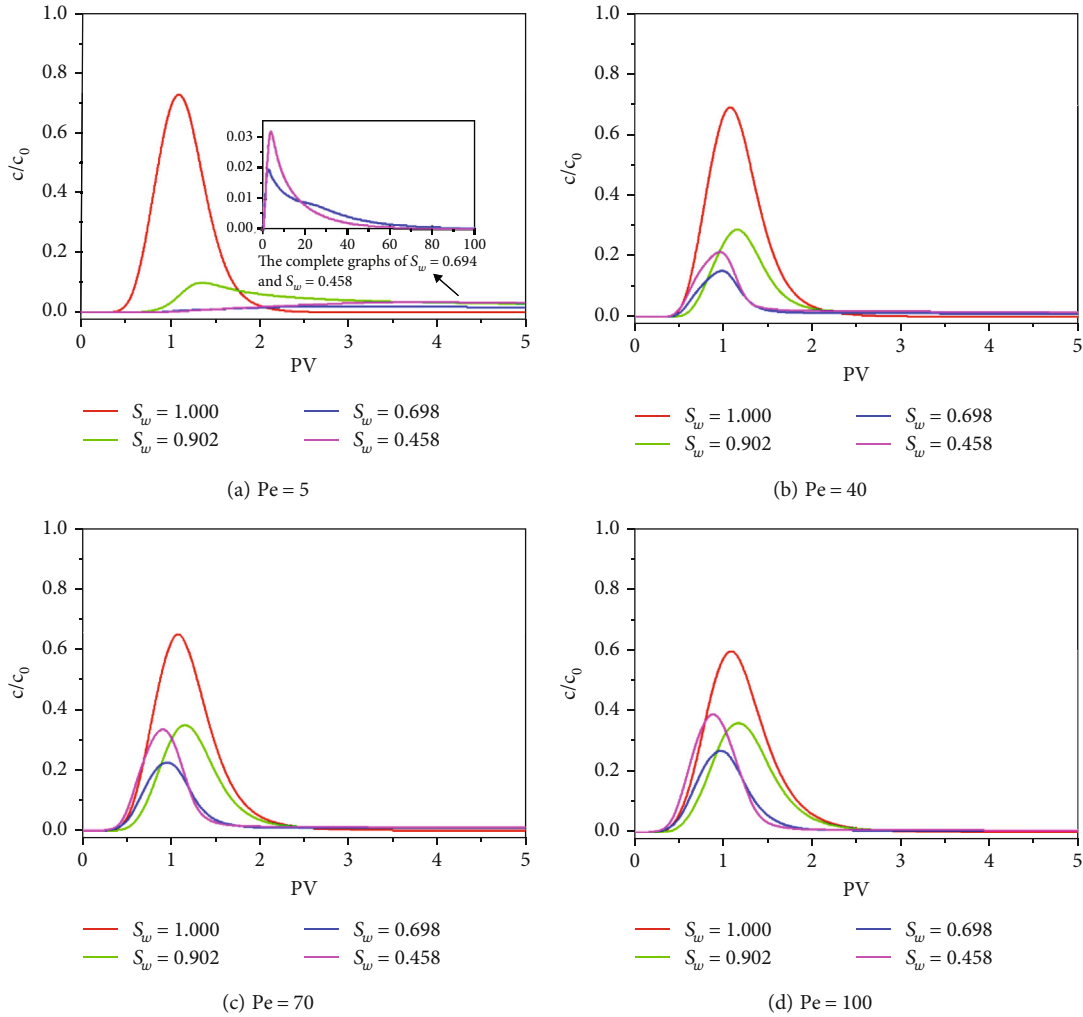


FIGURE 10: Breakthrough curves at different water saturations. The extended simulation time at Pe = 5 to 100 PV revealed the complete trend.

As can be seen in Figure 6, breakthrough curves follow a similar trend at different Peclet numbers. As the Peclet number increased, the arrival time was earlier. This is because advection was the primary mechanism of reactive solute transport. And at larger Peclet numbers, the flow was faster. It should be noted that the breakthrough curves exhibited left-right asymmetry and a significant tailing phenomenon. For the tailing phenomenon, the saturated and unsaturated curves were diametrically opposed. At unsaturated curves, the trailing phenomenon became more pronounced as the Peclet number decreased. In this study, solute chemistry and adsorption in saturated conditions were ignored, so the above phenomena were caused by the microscopic morphology of the pore structure and the inhomogeneous particles within the porous media. In unsaturated conditions, it was the result of a combination of adsorption reactions at the surface of the nonwetting liquid phase and the influencing variables in saturated media.

In order to quantitatively describe the influence of Peclet number on adsorption behavior at liquid-liquid interfaces, 500 PV of contaminate was injected to reach adsorption satu-

ration. The influence of adsorption within 10 PV was exhibited to clearly highlight the trend, as shown in Figure 7. The adsorbed amount at different Peclet numbers varied regularly with time and gradually increased to equilibrium as time increased. At early times, the adsorbed amount increased in a very similar way for all cases, and the adsorption rate decreased with increasing Peclet number. As time increased, the adsorption rate decreased, and the adsorption reached saturation. Table 3 shows the maximum adsorption and adsorption time at different Peclet numbers and water saturations. Further, we also plotted the maximum adsorption at different Peclet numbers as shown in Figure 8. It indicated that the Peclet number had little influence on the maximum adsorption. The adsorption time at saturation, on the other hand, increased with increasing Peclet number and showed a nearly linear relationship with the Peclet number. This is due to the fact that at higher velocities, the ability of solutes to penetrate the interface and experience adsorption is less than the transport capacity in the direction of water flow. Therefore, the adsorption rate is lower at higher flow velocities, and thus, more adsorption time is required.

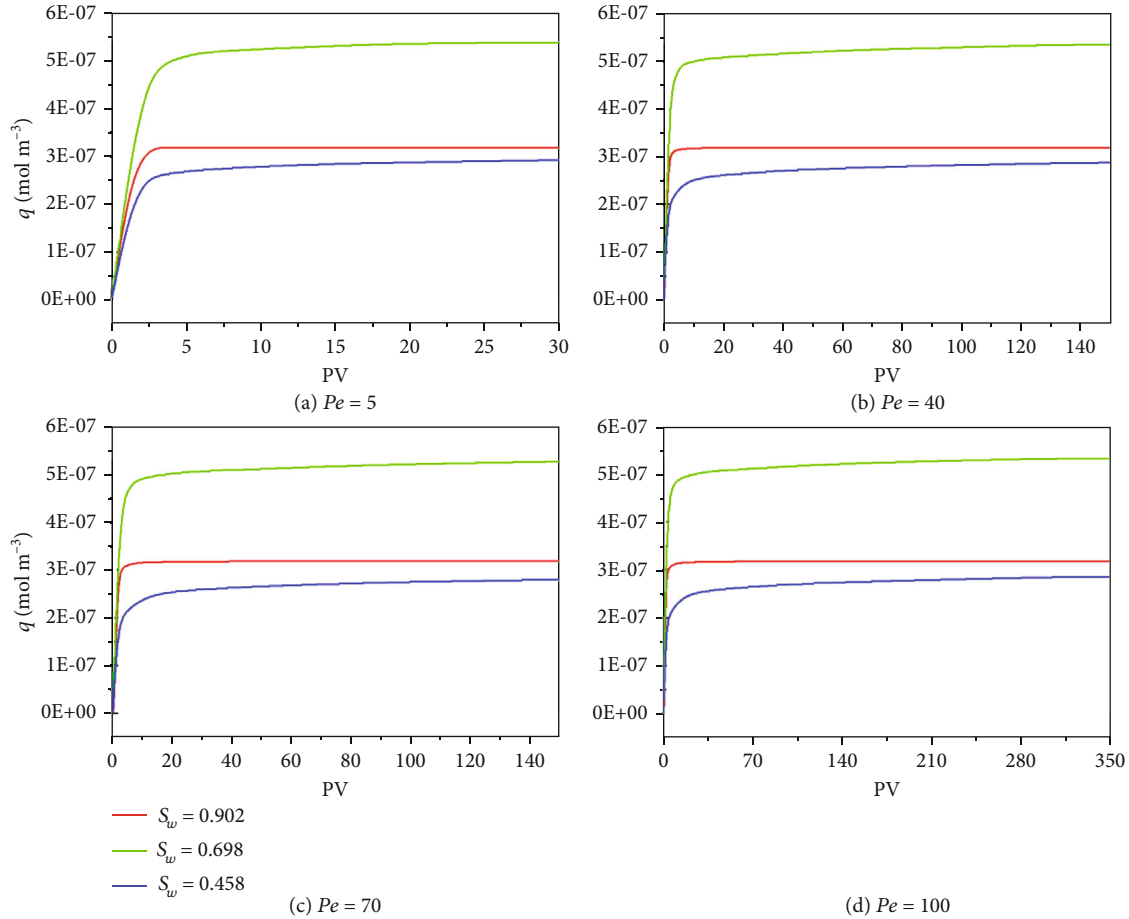


FIGURE 11: The influence of contact time on the adsorbed amount at different water saturations. In the early stage, the adsorbed amount increased in a very similar way, and the adsorption rate increased and then decreased with increasing water saturation.

3.3. Impact of Water Saturation on Adsorption Behavior at Liquid-Liquid Interfaces. The relevant parameters were determined as described above. Numerical simulations with constant PV were performed in four groups of geometric models with different water saturations ($S_w = 0.458$, $S_w = 0.698$, $S_w = 0.902$, and $S_w = 1.000$).

At the same Peclet number, as shown in Figure 9, it became clear that the same phenomenon of preferential flow occurred in reactive transport in the four different water saturation groups. In the less saturated geometric model, more fluids were in the nonwetting phase, resulting in a greater number of fronts with significant separation, compared to the more saturated geometric model in which there were fewer fronts without significant separation. Similarly, there were stationary and mobile zones as the water spread, resulting in strong stagnation.

Figure 10 clearly depicts the influence of the nonwetting phase fluid (TCE) and of the heterogeneity; it adds to the pore structure on reactive transport. The solute shows larger spreading, with earlier arrival times and a more pronounced tailing as water saturation decreases. This is due to the fact that with decreasing water saturation, more fronts existed in the unsaturated porous media, and reactive solute transport along the dominant channel became more obvious.

Although the internal heterogeneity resulted in strong lateral dispersion, the change in transport channels dominated in comparison, resulting in a decrease in transport time.

Similarly, we investigated the direct influence of saturation on adsorption behavior at liquid-liquid interfaces. The adsorbed amount at different water saturations is shown in Figure 11. In the early stage, the adsorbed amount increased in a very similar way, and the adsorption rate increased and then decreased with increasing water saturation. Figure 12(a) also shows a nonlinear relationship between the maximum adsorption and water saturation. The maximum adsorption tended to increase and then decrease as saturation increased. We explained this trend by finding a link with the area in porous media available for adsorption. It can be seen that the adsorption area tends to increase and then decrease with saturation as shown in Figure 12(b). This was consistent with the change in the maximum adsorption with saturation. The maximum adsorption at $S_w = 0.458$ exceeded that of $S_w = 0.698$ (the largest adsorption area), and this was thought to be due to the combined influence of the stationary zone and the preferential front. According to Table 3, the shortest adsorption times occurred in porous media with $S_w = 0.902$. Due to the microscopic morphology of the pore structure and the inhomogeneous particles within

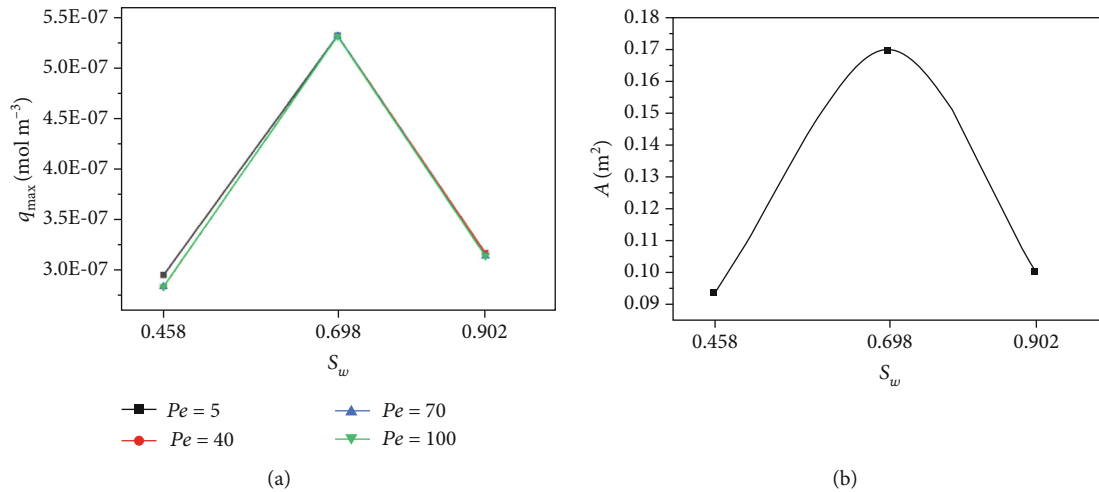


FIGURE 12: The maximum adsorption at different water saturations (a) and relationship between the adsorption area and water saturation (b). Their changes were consistent.

the porous media, $S_w = 0.458$ and $S_w = 0.698$ were substantially longer than those for $S_w = 0.902$. However, the difference in adsorption times for saturations of 0.458 and 0.698 was not significant and was only about 20 PV difference.

4. Conclusions

- (1) The complexity of the flow field was influenced by water saturation, and the uniformity of the flow showed a nonmonotonic relationship with water saturation. Quantitative evaluation of the CV and γ_v values showed that the uniformity of the flow field first increased and then decreased with decreasing water saturation
- (2) The Peclet number had little influence on the maximum adsorption. On the other hand, the adsorption time showed a nearly linear relationship with the Peclet number and increased with increasing Peclet number
- (3) A nonlinear relationship was found between water saturation and the maximum adsorption. With increasing water saturation, the maximum adsorption tended to increase to a peak and then decrease. The peak of the maximum adsorption occurred at $Pe = 5$, $S_w = 0.458$, and the shortest adsorption time was observed at $S_w = 0.902$. However, the difference in adsorption times for saturations of 0.458 and 0.698 was not significant and was only about 20 PV difference

Data Availability

The underlying data used to support the findings of this study are included within the article.

Conflicts of Interest

The authors declare that there is no conflict of interest regarding the publication of this paper.

Acknowledgments

The study is financially supported by the National Key Research and Development Program of China (No. 2019YFC1804300), the National Natural Science Foundation of China (Grant No. 42272278), and the China Scholarship Council (CSC202106710083).

References

- [1] K. H. Wei, J. Ma, B. D. Xi et al., "Recent progress on in-situ chemical oxidation for the remediation of petroleum contaminated soil and groundwater," *Journal of Hazardous Materials*, vol. 432, article 128738, 2022.
- [2] P. Mazumder, A. Das, M. Khwairakpam, and A. S. Kalamdhad, "A comprehensive insight into ecological risk assessment and remediation of metal contaminated coal mine soil: towards a cleaner and sustainable environment," *Journal of Cleaner Production*, vol. 324, article 129185, 2021.
- [3] C. Liu, X. Jiang, Y. Ma, and B. J. Cade-Menun, "Pollutant and soil types influence effectiveness of soil-applied absorbents in reducing rice plant uptake of persistent organic pollutants," *Pedosphere*, vol. 27, no. 3, pp. 537–547, 2017.
- [4] J. Li and Y. Ye, "Analysis of soil heavy metal pollution in Hechuan wetland," *Agricultural Science & Technology*, vol. 18, no. 1, p. 60, 2017.
- [5] S. Mishra, Z. Lin, S. Pang, Y. Zhang, P. Bhatt, and S. Chen, "Biosurfactant is a powerful tool for the bioremediation of heavy metals from contaminated soils," *Journal of Hazardous Materials*, vol. 418, article 126253, 2021.
- [6] C. V. Chrysikopoulos, P. K. Kitanidis, and P. V. Roberts, "Analysis of one-dimensional solute transport through porous media with spatially variable retardation factor," *Water Resources Research*, vol. 26, no. 3, pp. 437–446, 1990.

- [7] G. Sposito, V. K. Gupta, and R. N. Bhattacharya, "Foundation theories of solute transport in porous media: a critical review," *Advances in Water Resources*, vol. 2, pp. 59–68, 1979.
- [8] X. Yang, H. Sun, Y. Yang, Y. Liu, and X. Li, "Recent progress in multi-scale modeling and simulation of flow and solute transport in porous media," *WIREs Water*, vol. 8, no. 6, article e1561, 2021.
- [9] Y. Li, J. Bian, Q. Wang, and T. Li, "Experiment and simulation of non-reactive solute transport in porous media," *Groundwater*, vol. 60, no. 3, pp. 330–343, 2022.
- [10] A. X. Wu, C. Liu, S. H. Yin, Z. L. Xue, and X. Chen, "Pore structure and liquid flow velocity distribution in water-saturated porous media probed by MRI," *Transactions of Non-ferrous Metals Society of China*, vol. 26, no. 5, pp. 1403–1409, 2016.
- [11] M. Wang, H. Liu, D. Zak, and B. Lennartz, "Effect of anisotropy on solute transport in degraded fen peat soils," *Hydrological Processes*, vol. 34, no. 9, pp. 2128–2138, 2020.
- [12] X. P. Zhou and N. Xiao, "Analyzing fracture properties of the 3D reconstructed model of porous rocks," *Engineering Fracture Mechanics*, vol. 189, pp. 175–193, 2018.
- [13] Z. Liu, D. Liu, Y. Cai, Y. Yao, Z. Pan, and Y. Zhou, "Application of nuclear magnetic resonance (NMR) in coalbed methane and shale reservoirs: a review," *International Journal of Coal Geology*, vol. 218, article 103261, 2020.
- [14] B. Zhao, G. Wang, B. Wu, and X. Kong, "A study on mechanical properties and permeability of steam-cured mortar with iron-copper tailings," *Construction and Building Materials*, vol. 383, article 131372, 2023.
- [15] M. Luo, P. W. Glover, P. Zhao, and D. Li, "3D digital rock modeling of the fractal properties of pore structures," *Marine and Petroleum Geology*, vol. 122, article 104706, 2020.
- [16] Y. Zhao, X. Sun, T. Wen, R. Chen, and L. Huang, "Micro-structural evolution of granite residual soil under external loading based on X-ray micro-computed tomography," *KSCSE Journal of Civil Engineering*, vol. 25, no. 8, pp. 2836–2846, 2021.
- [17] S. Jiménez, R. Brauchler, R. Hu et al., "Prediction of solute transport in a heterogeneous aquifer utilizing hydraulic conductivity and specific storage tomograms," *Water Resources Research*, vol. 51, no. 7, pp. 5504–5520, 2015.
- [18] J. Niu and M. S. Phanikumar, "Modeling watershed-scale solute transport using an integrated, process-based hydrologic model with applications to bacterial fate and transport," *Journal of Hydrology*, vol. 529, pp. 35–48, 2015.
- [19] L. Budinski, "Solute transport in shallow water flows using the coupled curvilinear lattice Boltzmann method," *Journal of Hydrology*, vol. 573, pp. 557–567, 2019.
- [20] M. Morales-Hernández, J. Murillo, and P. García-Navarro, "Diffusion–dispersion numerical discretization for solute transport in 2D transient shallow flows," *Environmental Fluid Mechanics*, vol. 19, no. 5, pp. 1217–1234, 2019.
- [21] D. Costa, K. Shook, C. Spence et al., "Predicting variable contributing areas, hydrological connectivity, and solute transport pathways for a Canadian Prairie basin," *Water Resources Research*, vol. 56, no. 12, article e2020WR027984, 2020.
- [22] A. L. Harrison, G. M. Dipple, I. M. Power, and K. U. Mayer, "Influence of surface passivation and water content on mineral reactions in unsaturated porous media: implications for brucite carbonation and CO₂ sequestration," *Geochimica et Cosmochimica Acta*, vol. 148, pp. 477–495, 2015.
- [23] A. L. Harrison, G. M. Dipple, I. M. Power, and K. U. Mayer, "The impact of evolving mineral-water-gas interfacial areas on mineral-fluid reaction rates in unsaturated porous media," *Chemical Geology*, vol. 421, pp. 65–80, 2016.
- [24] A. Raoof, H. M. Nick, S. M. Hassanizadeh, and C. J. Spiers, "PoreFlow: a complex pore-network model for simulation of reactive transport in variably saturated porous media," *Computers & Geosciences*, vol. 61, pp. 160–174, 2013.
- [25] J. Jiménez-Martínez, P. D. Anna, H. Tabuteau, R. Turuban, T. L. Borgne, and Y. Méheust, "Pore-scale mechanisms for the enhancement of mixing in unsaturated porous media and implications for chemical reactions," *Geophysical Research Letters*, vol. 42, no. 13, pp. 5316–5324, 2015.
- [26] A. J. Valocchi, D. Bolster, and C. J. Werth, "Mixing-limited reactions in porous media," *Transport in Porous Media*, vol. 130, no. 1, pp. 157–182, 2019.
- [27] Z. Dou, X. Zhang, C. Zhuang, Y. Yang, J. Wang, and Z. Zhou, "Saturation dependence of mass transfer for solute transport through residual unsaturated porous media," *International Journal of Heat and Mass Transfer*, vol. 188, article 122595, 2022.
- [28] L. Yue, C. Ge, D. Feng, H. Yu, H. Deng, and B. Fu, "Adsorption-desorption behavior of atrazine on agricultural soils in China," *Journal of Environmental Sciences*, vol. 57, pp. 180–189, 2017.
- [29] D. Lyu, Y. B. Mollamahale, S. Huang et al., "Ultra-high surface area graphitic Fe-N-C nanospheres with single-atom iron sites as highly efficient non-precious metal bifunctional catalysts towards oxygen redox reactions," *Journal of Catalysis*, vol. 368, pp. 279–290, 2018.
- [30] Z. Dou, X. Zhang, Z. Chen, Y. Yang, C. Zhuang, and C. Wang, "Effects of cemented porous media on temporal mixing behavior of conservative solute transport," *Water*, vol. 11, no. 6, p. 1204, 2019.
- [31] A. Saif, R. R. William, B. A. Daryl, and Z. Hailin, "Prediction of maize (*Zea mays* L.) population using normalized-difference vegetative index (NDVI) and coefficient of variation (CV)," *Journal of Plant Nutrition*, vol. 42, no. 6, pp. 673–679, 2019.
- [32] S. Jafaradar, H. Taghavifar, H. Taghavifar, and A. Navid, "Numerical assessment of flow dynamics for various DI diesel engine designs considering swirl number and uniformity index," *Energy Conversion and Management*, vol. 110, pp. 347–355, 2016.